Surface Albedo over the Arctic Ocean Derived from AVHRR and Its Validation with SHEBA Data

XIAOZHEN XIONG

Geophysical Institute, University of Alaska Fairbanks, Fairbanks, Alaska

KNUT STAMNES

Stevens Institute of Technology, Hoboken, New Jersey

DAN LUBIN

Scripps Institution of Oceanography, University of California, San Diego, La Jolla, California

(Manuscript received 23 April 2001, in final form 5 November 2001)

ABSTRACT

A method is presented for retrieving the broadband albedo over the Arctic Ocean using advanced very high resolution radiometer (AVHRR) data obtained from NOAA polar-orbiting satellites. Visible and near-infrared albedos over snow and ice surfaces are retrieved from AVHRR channels 1 and 2, respectively, and the broadband shortwave albedo is derived through narrow-to-broadband conversion (NTBC). It is found that field measurements taken under different conditions yield different NTBC coefficients. Model simulations over snow and ice surfaces based on rigorous radiative transfer theory support this finding. The lack of a universal set of NTBC coefficients implies a 5%–10% error in the retrieved broadband albedo. An empirical formula is derived for converting albedo values from AVHRR channels 1 and 2 into a broadband albedo under different snow and ice surface conditions. Uncertain calibration of AVHRR channels 1 and 2 is the largest source of uncertainty, and an error of 5% in satellite-measured radiance leads to an error of 5%–10% in the retrieved albedo. *NOAA-14* AVHRR data obtained over the Surface Heat Budget of the Arctic Ocean (SHEBA) ice camp are used to derive the seasonal variation of the surface albedo over the Arctic Ocean between April and August of 1998. Comparison with surface measurements of albedo by Perovich and others near the SHEBA ice camp shows very good agreement. On average, the retrieval error of albedo from AVHRR is 5%–10%.

1. Introduction

Surface albedo is one of the most important factors influencing the radiation budget of the earth–atmosphere system (e.g., Curry et al. 1996; Stamnes et al. 1999, and references therein). Of all the surface types on the earth, snow and ice surfaces have the highest albedo. The bidirectional reflectance over snow or ice surfaces is pronounced for the large solar zenith angles encountered in the Arctic (Han et al. 1999). Thus, accurate determination of the albedo and the bidirectional reflectance distribution function (BRDF) is essential for reliable estimation of the radiation budget in the Arctic. However, the continuous solar illumination during the summer results in a rapid change of the surface physical conditions, such as the melting of snow and ice, and the formation of ponds and leads. This season between May and August in the Arctic, characterized by rapid change of surface physical conditions, is called the ''transition season.'' The rapid change of surface albedo due to the fast change of surface conditions and the scarcity of field measurements of albedo make it difficult to ascertain the albedo with an accuracy sufficient for testing and improving the performance of climate model simulations in the Arctic. Measurements over large spatial areas from satellites and the frequent overpasses of polar-orbiting satellites in the polar regions, however, make it feasible to monitor the change of the surface albedo and BRDF from space.

The snow/ice albedo generally depends on the wavelength of the incident solar radiation; snow grain size; air bubble distribution; solar zenith angle; cloud cover; and impurities such as dust, ash, soot, and salt (Clarke and Noone 1985; Warren 1982; Tsay et al. 1989). As the snow ages, the grain size increases and thus lowers the albedo. Retrieval of surface albedo from satellite-measured radiances has been attempted for many years, but most attempts were made over non-snow-covered

Corresponding author address: Knut Stamnes, Light and Life Laboratory, Department of Physics and Engineering Physics, Castle Point on Hudson, Stevens Institute of Technology, Hoboken, NJ 07030.
E-mail: kstamnes@stevens-tech.edu

land surfaces (e.g., Langleben 1971; Briegleb et al. 1986; Saunders 1990; Toll et al. 1997; Csiszar and Gutman 1999; Song and Gao 1999). Surface albedo has been derived over snow/ice surfaces using advanced very high resolution radiometer (AVHRR) data by De Abreu et al. (1994), Li and Leighton (1992), Lindsay and Rothrock (1994), Knap and Oerlemans (1996), Stroeve et al. (1997), and Knap et al. (1999). However, ground-based measurements of albedo in the Arctic that can be used for validation purposes are scarce. Also, cloud-masking techniques used to identify clear pixels over snow and ice surfaces were unreliable in the past (Xiong 2000), and problems still exist in the cloud-masking procedure for the AVHRR polar pathfinder product. Thus, progress in this area of research depends on improvement and validation of surface albedo retrieval over high-albedo surfaces.

In this paper, we present an algorithm based on lookup tables to retrieve narrowband albedo for AVHRR channels 1 and 2. Anisotropic correction is made for highly reflecting snow surfaces, which exhibit appreciable bidirectional reflectance. A narrow-to-broadband-conversion (NTBC) scheme, based on a rigorous radiative transfer model and surface measurements, is used to derive the broadband albedo. This algorithm is employed to derive the seasonal variation of albedo over the Arctic Ocean. Very good agreement is obtained with the Surface Heat Budget of the Arctic Ocean (SHEBA) surface measurements of albedo reported by Perovich et al. (1999).

2. Retrieval methods

a. Radiative transfer model (RTM)

The radiative transfer model used here is the discrete ordinate method as implemented numerically in the discrete ordinate radiative transfer (DISORT) code (Stamnes et al. 1988; Thomas and Stamnes 1999). The atmosphere is assumed to consist of multiple adjacent plane-parallel homogeneous layers in which the single-scattering properties are constant within each layer but may vary from layer to layer. Molecular scattering is computed from Rayleigh scattering theory (Penndorf 1957; Thomas and Stamnes 1999). Band models are efficient and convenient tools for computing the spectral dependence of the solar and thermal infrared atmospheric radiation. For example, the solar spectrum between 0.28 and 4 μm may be divided into 24 bands with unequal spectral widths varying from 240 to 2040 cm^{-1} (Tsay et al. 1989, 1990). Because the channel response function and the channel width of satellite sensors are not exactly consistent with that used in the 24 bands, the moderate-resolution atmospheric radiance and transmittance model and code (MODTRAN) with 2 cm^{-1} is used to compute clear-sky optical depth profiles for atmospheric absorbers such as water vapor, methane, ozone, nitrous oxide, carbon monoxide, and carbon dioxide and for aerosols. Lacking better information, the tropospheric background aerosol model is frequently used in the Arctic because the volume extinction coefficient of Arctic haze is similar to that of tropospheric aerosols (Blanchet and List 1983; Han et al. 1999).

A subarctic model atmosphere (McClatchey et al. 1971; Anderson et al. 1986) is employed but the atmospheric temperature distribution and water vapor profile are taken from in situ sounding data. The lower boundary is treated as follows: for snow-free conditions, the surface is treated as a Lambert reflector with an assigned albedo; under snow-covered conditions, an additional layer of snow is added at the bottom of the atmosphere to represent snow overlying tundra (or sea ice). Optical properties of snow are adopted from Warren and Wiscombe (1980) and Warren (1982).

b. Retrieval of narrowband albedo

Satellite sensors measure the radiance at the top of the atmosphere (TOA), which depends on the surface reflectance and the effects of the intervening atmosphere. For each AVHRR channel, we solve the radiative transfer equation subject to appropriate boundary conditions. Let us assume that the optical properties of the atmosphere due to gases and aerosols are known from climatological data and that multiple scattering in the atmosphere and multiple reflections between the atmosphere and the surface can be accurately computed with RTMs. Then, the only unknown variable is the surface albedo if the surface is assumed to be a Lambert reflector whose reflectance is uniform (independent of angle). In general, the reflectance at the TOA increases with increasing surface albedo (for a Lambertian surface) if the optical properties of gases and aerosols in the atmosphere are kept constant. Thus, the surface albedo can be determined uniquely from TOA satellite-measured radiances. The narrowband albedo can be retrieved with sufficient accuracy for Lambertian surfaces if the atmospheric optical properties are known and the radiances are measured accurately.

In general, derivation of surface narrowband albedo from satellite data requires (i) conversion of directional reflectance to hemispherically integrated reflectance or albedo and (ii) removal of atmospheric effects. To account for atmospheric effects, a relationship is usually derived between the satellite measurements and the surface albedo. Thus, a linear relationship between the narrowband surface albedo and the TOA albedo was derived for AVHRR channels 1 and 2 by Koepke (1989). This relationship had different coefficients for discrete aerosol optical depths, ozone and water vapor amounts, and solar zenith angles. Koepke's method has been applied with some success to derive the albedo from AVHRR data in the polar regions by de Abreu et al. (1994), Lindsay and Rothrock (1994), and Knap and Oerlemans (1996). Stroeve et al. (1997) found that

Koepke's method underestimated the visible albedo by 3.9% and overestimated the near-infrared albedo by 5.9%, however. Stroeve et al. (1997) used an RTM to calculate the transmittance, spherical reflectance, and atmospheric reflectance, and the surface albedo was represented as a function of satellite-measured reflectance and the above variables. This method was used to derive surface albedo over Greenland (Stroeve et al. 1997, 2001). A more straightforward method that relies on the use of a state-of-the-art RTM, briefly described above, is developed in this paper. We use the RTM to generate lookup tables of the TOA reflectance in channels 1 and 2 as a function of solar zenith angle, viewing angle, relative azimuthal angle, and surface albedo. Use of lookup tables generated in this manner to retrieve atmospheric and surface properties from satellite data has been investigated by Han et al. (1999). The advantage of this approach is that the atmospheric radiative transfer process can be described accurately by the RTM. The atmospheric optical properties in the RTM are based on climatological data (aerosol optical depth and the amounts of ozone and water vapor) and the surface is assumed to be a Lambertian reflector. The lookup tables include nine surface albedos ranging from 0.05 to 0.9, 10 solar zenith angles θ_0 ranging from 35° to 70°, and 10 viewing angles θ ranging from 0° to 65°. To account for the variation of the reflectance with the relative azimuthal angle ϕ, 10 terms in a Fourier expansion of the TOA reflectance with azimuthal angle are used to compute the reflectance for any required azimuthal angle. This method is more accurate than using interpolation in azimuth, as shown by Lubin and Weber (1995). Thus, for a given sun–satellite geometry (solar zenith angle, viewing angle, and relative azimuthal angle), we can, through linear interpolation in the lookup tables, generate new tables of the TOA reflectances versus surface albedo in AVHRR channels 1 and 2. For a given TOA reflectance, narrowband albedos in AVHRR channels 1 and 2 are retrieved individually by interpolation.

c. Anisotropic correction

Because there is a strong bidirectional reflectance of snow and ice surfaces in the polar regions, an ''anisotropic correction'' to the hypothetical albedo (isotropic) ''retrieved'' from satellite-measured reflectance is necessary. To account for the bidirectional reflectance, an anisotropic reflectance factor (ARF) or so-called anisotropic reflection function is generally used (e.g., Taylor and Stowe 1984; Suttles et al. 1988; Lindsay and Rothrock 1994; Stroeve et al. 1997). ARF is defined as:

$$\mathrm{ARF}(\theta_0, \theta, \phi) = \frac{\pi R(\theta_0, \theta, \phi)}{\alpha_{\mathrm{ac}}(\theta_0)},$$

where $R(\theta_0, \theta, \phi)$ is the BRDF. The actual albedo $\alpha_{\mathrm{ac}}(\theta_0)$ depends only on solar zenith angle and is independent of polar (viewing) angle and the relative azimuthal angle. The ARF is unity if the reflected radiation is uniform over the downward hemisphere (independent of viewing angle), but, in general, it represents the departure of the reflected radiation field from a uniform angular distribution. Large variations in the albedo at the TOA are frequently encountered over snow and ice surfaces (e.g., Jin and Simpson 1999, 2000; Stroeve et al. 1997). Thus, the ''isotropic'' albedo $\alpha(\theta_0, \theta, \phi)$ retrieved from the satellite-measured radiance by assuming that reflected radiation is uniform over the downward hemisphere will depend on solar zenith angle, viewing angle, and azimuthal angle. For a specific set of angles θ_0, θ, and ϕ, this isotropic albedo can be converted into the actual (''true'') albedo through division by the ARF, as follows:

$$\alpha_s \equiv \alpha_{\mathrm{ac}}(\theta_0) = \frac{\alpha(\theta_0, \theta, \phi)}{\mathrm{ARF}(\theta_0, \theta, \phi)}. \quad (1)$$

Thus, if the ARF is greater than 1, the satellite-retrieved albedo obtained by invoking the Lambertian assumption overestimates the true albedo, and if the ARF is less than 1, it underestimates the true albedo (Stroeve et al. 1997).

Broadband ARFs have been compiled by Taylor and Stowe (1984) for a variety of different surfaces and clouds using *Nimbus-7* Earth Radiation Budget (ERB) data. An improvement was made by Suttles et al. (1988) using *Nimbus-7* ERB data and Geostationary Operational Environmental Satellite data. These ARFs were derived for the broadband albedo, so they can be applied to AVHRR channels 1 and 2 only if we assume that the broadband ARFs are applicable also to these two channels (de Abreu et al. 1994). However, Lubin and Weber (1995) have shown that this is generally not the case. Aoki et al. (2000) found that the anisotropic reflection was very significant in the near-infrared while the pattern of ARF was relatively flat in the visible. Jin and Simpson (1999, 2000) also pointed out that the reflectance anisotrophy is larger in AVHRR channel 2 than in channel 1. Stroeve et al. (2001) recently found through comparisons with surface albedo data obtained in Greenland that the Lindsay and Rothrock (1994) model does not account adequately for the variation of snow albedo with sensor viewing angle and relative azimuthal angle. Because correction of narrowband albedo in channels 1 and 2 requires the ARF for each of the two channels, we use an RTM for the coupled atmosphere–snow surface system to calculate the ARF assuming that the surface consists of a homogeneous layer of snow with optical properties depending on effective snow grain size and impurities (Warren and Wiscombe 1980; Warren 1982). This approach is similar to that used by Stroeve et al. (1997) and by Jin and Simpson (2000) to generate anisotropic reflectance factors for snow surfaces.

Because the surface is covered by homogeneous fine-grain snow over ice before the onset of melting in mid- to late June, an assumption of a homogeneous snow

layer seems appropriate. From analysis of 50 AVHRR images from between the middle of April and the end of May, we found that, without anisotropic correction, the albedo can be underestimated or overestimated by as much as 20%; on average, it is underestimated by about 10%. However, with the melting of snow and ice, the surface becomes highly inhomogeneous in late summer, consisting of a composite of melting snow, ponds, and leads. To make corrections based on ARFs over snow surfaces may cause an underestimate or an overestimate of the albedo. Because our knowledge of ARFs is poor after the surface becomes highly inhomogeneous, the Lambertian assumption becomes appropriate. Therefore, we make anisotropic corrections to the retrieved albedo in channels 1 and 2 before 10 June 1998, and after that the surface is assumed to be a Lambertian reflector. This assumption leads to acceptable results if the viewing angle is close to nadir as discussed below.

d. Narrow-to-broadband conversion

Because the AVHRR sensors measure the narrowband directional radiance only in 2 channels (0.58–0.68 and 0.725–1.1 μm), we can derive the albedo from the satellite-measured radiances only in those two specific channels. However, at present most global and/or regional climate models require the broadband albedo. Thus, it is desirable to derive the surface broadband albedo by conversion from narrowband to broadband albedo. In general, this conversion consists of a linear regression of the spectral surface albedos in AVHRR channels 1 and 2. Several investigators have attempted to derive albedo of snow surfaces from AVHRR data. They include Li and Leighton (1992), Stroeve et al. (1997), and Knap et al. (1999). However, distinct characteristics of the albedo in the visible and near-infrared regions for different surface conditions may require different NTBC coefficients (Song and Gao 1999).

The broadband surface albedo α is defined as the fraction of the downward solar irradiance incident on the surface that is reflected. Thus, it can be expressed as follows:

$$\alpha = \frac{\sum_i \alpha_i F_i}{\sum_i F_i} = \alpha_{\rm VIS}\frac{F_{\rm VIS}}{\sum_i F_i} + \alpha_{\rm NIR}\frac{F_{\rm NIR}}{\sum_i F_i} + \alpha_{\rm IR}\frac{F_{\rm IR}}{\sum_i F_i}$$

$$= B_1\alpha_{\rm VIS} + B_2\alpha_{\rm NIR} + B_0.$$

Here,

$$B_1 = \frac{F_{\rm VIS}}{\sum_i F_i}, \qquad B_2 = \frac{F_{\rm NIR}}{\sum_i F_i}, \quad \text{and}$$

$$B_0 = \alpha_{\rm IR}\frac{F_{\rm IR}}{\sum_i F_i}, \tag{2}$$

where F_i is the downward irradiance in band i; $F_{\rm VIS}$ and $F_{\rm NIR}$ are the downward irradiances in the visible (0.35–0.75 μm) and near-infrared (NIR; 0.75–2.8 μm), respectively; and $\alpha_{\rm VIS}$ and $\alpha_{\rm NIR}$ are the narrowband albedo in the visible and near-infrared, respectively. Because the albedo over snow and ice surfaces decreases greatly for wavelengths larger than 1.40 μm (see Fig. 11 of Aoki et al. 2000), the last term B_0 is small and can be assumed to be constant. In our model simulations, the bands we used are exactly the same as AVHRR channels 1 (0.58–0.68 μm) and 2 (0.725–1.10 μm).

If we assume that the albedo in the visible is close to the albedo in AVHRR channel 1 (0.58–0.68 μm; α_1) and that the albedo in the near-infrared is close to the albedo in AVHRR channel 2 (0.725–1.10 μm; α_2), we can write:

$$\alpha = C_1\alpha_1 + C_2\alpha_2 + C_0.$$

Here,

$$C_1 = \frac{\alpha_{\rm VIS}}{\alpha_1}B_1 = \frac{F^{\rm up}_{\rm VIS}}{F_{\rm VIS}}\frac{F_1}{F^{\rm up}_1}\frac{F_{\rm VIS}}{\sum_i F_i} = \frac{F^{\rm up}_{\rm VIS}}{F^{\rm up}_1}\frac{F_1}{\sum_i F_i},$$

$$C_2 = \frac{\alpha_{\rm NIR}}{\alpha_2}B_2 = \frac{F^{\rm up}_{\rm NIR}}{F^{\rm up}_2}\frac{F_2}{\sum_i F_i}, \quad \text{and} \quad C_0 = B_0, \tag{3}$$

where F_1 and F_2 are the downward surface irradiance in AVHRR channels 1 and 2 and $F^{\rm up}_1$ and $F^{\rm up}_2$ are the corresponding upward surface irradiance in channels 1 and 2, respectively.

In the physical world, C_1 and C_2 are complicated nonlinear functions of atmospheric parameters and surface conditions because the spectral transmittance in channels 1 and 2 is influenced by the complicated process of scattering and absorption in the atmosphere by aerosols, water vapor, and other trace gases; multiple reflections between the atmosphere and the underlying surface; and the absorption at the surface. From Eq. (3), the C_1 coefficient is the ratio of downward solar irradiance in channel 1 to the total downward solar irradiance multiplied by the ratio of upward irradiance in the visible to that in channel 1. The ratio of the upward irradiance in the visible to that in channel 1 and the ratio of the upward irradiance in the NIR to that in channel 2 are both almost constant because channels 1 and 2 cover the main portions of the visible and near-infrared spectral regions, respectively. Thus, C_1 is mainly determined by the ratio of downward solar irradiance in channel 1 to the total downward solar irradiance. For this reason, C_1 can be taken as the ratio of the irradiance in channel 1 to the total downward solar irradiance, and C_2 can be taken as the ratio of the irradiance in channel 2 to the total downward solar irradiance, multiplied by a constant. As an approximation, C_1 and C_2 are usually assumed to be constant for a specific atmosphere–surface condition, and the broadband albedo is represented approximately as a linear function of spectral albedo in channels 1 and 2. In general, we expect that use of two

TABLE 1. NTBC over snow and ice surfaces.

Source	NTBC	Surface type
Lindsay and Rothrock (1994)	$\alpha = 0.43\alpha_1 + 0.47\alpha_2$	Antarctic
Stroeve et al. (1997)	$\alpha = 0.041\ 23 + 0.655\alpha_1 + 0.216\alpha_2$	Greenland ice sheet
Li and Leighton (1992)	$\alpha = 0.0453 + 0.389\alpha_1 + 0.452\alpha_2$	TOA (over snow/ice)
Xiong (2000)	$\alpha = 0.007 + 0.542\alpha_1 + 0.340\alpha_2$	SHEBA [data from Perovich et al. (1999)]
Xiong (2000)	$\alpha = 0.007 + 0.434\alpha_1 + 0.464\alpha_2$	Snow surface (model)
Xiong (2000)	$\alpha = 0.045 + 0.304\alpha_1 + 0.486\alpha_2$	TOA (model)
Xiong (2000)	$\alpha = 0.28(1+ 8.26\gamma)\alpha_1 + 0.63(1 - 3.96\gamma)\alpha_2 + 0.22\gamma - 0.009$, $\gamma = (\alpha_1 - \alpha_2)/(\alpha_1 + \alpha_2)$	Snow/ice

AVHRR channels should give an overall higher accuracy than using just one of them to estimate the broadband albedo. The reason is that the broadband albedo is influenced by variations in both surface and atmospheric conditions, which affect the whole shortwave region. Thus, we expect the two AVHRR channels to capture these variations better than either one of them alone. Stroeve et al. (1997) pointed out that use of both channels increases the accuracy of the broadband albedo estimate (accuracy of 0.66%) and explains approximately 98.5% of the variance associated with surface broadband albedo. However, C_1 and C_2 will depend on atmospheric conditions and surface optical properties. Song and Gao (1999) recently developed an NTBC conversion scheme in which C_1 and C_2 are represented as a function of the vegetation index of land surfaces. An empirical relationship was established on the basis of multiple linear regression analysis of 112 ground-based simultaneous measurement of broadband albedo and narrowband albedos in channels 2 (0.56–0.60 μm) and 4 (0.76–0.90 μm) at various sites on the Morteratschgletscher (Switzerland) during winter, spring, and summer (Knap et al. 1999). In this relationship, the broadband albedo is calculated as a second-order polynomial of the narrowband albedos in Landsat thematic mapper channels 2 and 4.

In situ observations of albedo over snow and ice surfaces show that there are considerable discrepancies between the NTBC coefficients derived from different experiments over snow and ice surfaces. In Table 1 we list several NTBC conversion coefficients that have been derived. Those of Stroeve et al. (1997) are based on measurements obtained on the midwestern slope of the Greenland ice sheet, whereas Lindsay and Rothrock (1994) used measurements for snow-covered ice in the east Antarctic reported by Allison et al. (1993). The discrepancies between the Stroeve et al. and Lindsay and Rothrock results must be due to different surface and atmospheric conditions at the two measurement sites. Because the variation of clear-sky atmospheric variables that influence the transmittance of solar radiation is relatively small in the Arctic (except for water vapor) and simultaneous measurements of surface albedo and atmospheric transmittance are scarce, we focus on the derivation of surface albedo under changing surface conditions throughout the melting season. The relation of Li and Leighton (1992) was derived for NTBC at the TOA. More weight is given to channel 1 in the relation of Stroeve et al. as compared with that of Li and Leighton. Stroeve et al. (1997) pointed out that use of the relation of Li and Leighton led to an estimated surface broadband albedo that on average is 4.5% lower than the broadband albedo observed at the surface.

If we ignore the variation in atmospheric conditions, the increase in surface albedo leads to an increase of the downward shortwave irradiance because multiple reflections between the surface and the atmosphere increase with increasing surface albedo. This relation can be illustrated based on the monochromatic transmittance $T_j(\tau_j, \mu_0, \alpha_j^s)$ for a plane-parallel atmosphere overlying a Lambert surface of albedo α_j^s expressed exactly as (Stamnes 1982)

$$T_j(\tau_j, \mu_0, \alpha_s) = \frac{T_j(\tau_j, \mu_0, \alpha_j^s = 0)}{1 - \alpha_j^s \overline{\alpha_j}}.$$

The subscript j designates the wavelength, $T_j(\tau_j, \mu_0, \alpha_j^s = 0)$ is the spectral transmittance for a "black" surface ($\alpha_j^s = 0$), μ_0 is the solar zenith angle, and τ_j is the optical depth. Note that $\overline{\alpha_j}$ is the spherical albedo of the atmosphere for illumination from *below* (see Stamnes 1982; Thomas and Stamnes 1999). Because the denominator decreases with surface albedo α_j^s while the numerator is independent of α_j^s by definition, the transmittance $T_j(\tau_j, \mu_0, \alpha_s)$ increases with surface albedo. When the snow and ice surface starts melting, the spectral albedo decreases much more in channel 2 than in channel 1 because of the strong absorption of near-infrared radiation by water. This result implies that the change in F_1 is small, whereas F_2 decreases significantly. Hence, the decrease of ΣF_i is smaller than that of F_2 but larger than that of F_1. According to Eq. (3), C_1 will increase and C_2 will decrease with the melting of snow and ice.

This expectation can be tested using the SHEBA surface measurements. At SHEBA, Perovich et al. (1999)

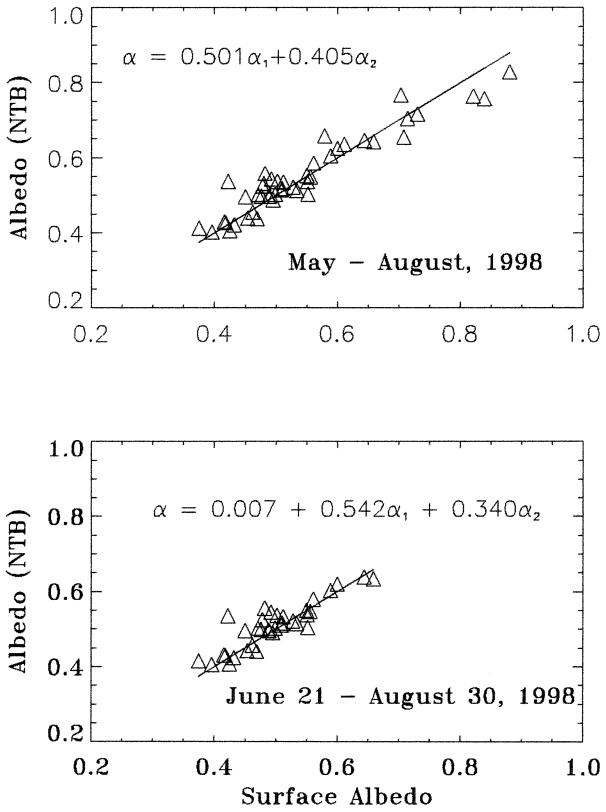

FIG. 1. NTBC relation derived by linear regression using SHEBA surface measurement of albedos (Perovich et al. 1999) (top) in the whole season from May to Aug (number of measurements $N = 45$) and (bottom) after the melting of snow and ice from 21 Jun to 30 Aug ($N = 35$). After snow melting, C_1 increases and C_2 decreases [Eq. (3)]. The x axis is the measured broadband albedo and the y axis is the derived broadband albedo via NTBC.

measured albedo along a 200-m survey line consisting of snow/ice conditions that changed as the melting progressed. We took the average of the albedo along the survey line as representing the average condition of the surface viewed from space. Using 45 surface measurements of Perovich et al. (1999) taken between May and August of 1998, we performed a linear regression between the broadband albedo and the spectral albedos centered at 0.63 and 0.86 μm and obtained

$$\alpha = 0.501\alpha_1 + 0.405\alpha_2. \quad (4)$$

To examine the dependence of the NTBC coefficients after the onset of snowmelt, we made a linear regression based on 35 surface measurements from between 20 June and 30 August 1998 and obtained

$$\alpha = 0.007 + 0.542\alpha_1 + 0.340\alpha_2. \quad (5)$$

We note that in Eq. (5) the coefficient C_1 is larger than and C_2 is smaller than the corresponding ones in Eq. (4), in agreement with expectations.

Comparison of surface albedo measured by Perovich et al. (1999) with the albedo estimated by the NTBC relations derived above is shown in Fig. 1. A good fit is obtained for the whole melting season with a relative error of 5% and a standard deviation of 0.04. As the surface conditions evolved from dry snow (April–May), to melting snow (3 June), to early melt ponds (mid- to late June), to fully developed melt ponds (July–August; Perovich et al. 1999), the albedo in channel 2 decreases faster than that in channel 1 because the reflectance over melting ice or ponds in the near-infrared is much smaller than that over a snow surface. Thus, the contribution of channel 2 to the broadband albedo becomes smaller, resulting in a smaller value of the C_2 NTBC coefficient. Because there are only a few measurements by Perovich et al. (1999) over snow surfaces before the onset of snowmelt in June, we used the RTM to simulate the spectral albedos in channels 1 and 2 and the corresponding broadband albedo for a series of snow grain sizes, mass fractions of soot, and solar zenith angles in the Arctic. Using a linear regression we found the following relationships between the narrowband and broadband albedo at the snow surface:

$$\alpha = 0.007 + 0.434\alpha_1 + 0.464\alpha_2; \quad (6)$$

and at the TOA:

$$\alpha = 0.045 + 0.304\alpha_1 + 0.486\alpha_2. \quad (7)$$

Figure 2 shows a comparison of the broadband surface albedo obtained directly from the model simulations and that derived from the NTBC using the model-simulated narrowband albedos in AVHRR channels 1 and 2. The discrepancy between the model-simulated broadband albedo and that derived from the NTBC is about 2%. The model-derived NTBC relationship over a snow surface is close to that obtained for Antarctic snow by Lindsay and Rothrock (1994). Model simulations also demonstrate that, with increase of the mass fraction of soot in the snow, C_1 increases and C_2 decreases. The disagreement between the various NTBC coefficients implies that broadband albedo values, inferred from satellite data in the polar regions based on the use of a single set of NTBC coefficients, may have large uncertainties.

Based on the surface measurements of Perovich et al. (1999) and model simulations over snow surfaces, we derived the following empirical NTBC relationship:

$$\alpha = 0.28(1 + 8.26\gamma)\alpha_1 + 0.63(1 - 3.96\gamma)\alpha_2 + 0.22\gamma - 0.009, \quad (8)$$

where

$$\gamma = \frac{\alpha_1 - \alpha_2}{\alpha_1 + \alpha_2}.$$

Because the albedo in the visible is close to that in the NIR over snow surfaces, and the decrease of albedo in the NIR is much larger than in the visible over ice or ponds, γ can be thought of as representing the change in surface conditions associated with snowmelt. Thus, a low value of γ is indicative of fresh snow, whereas

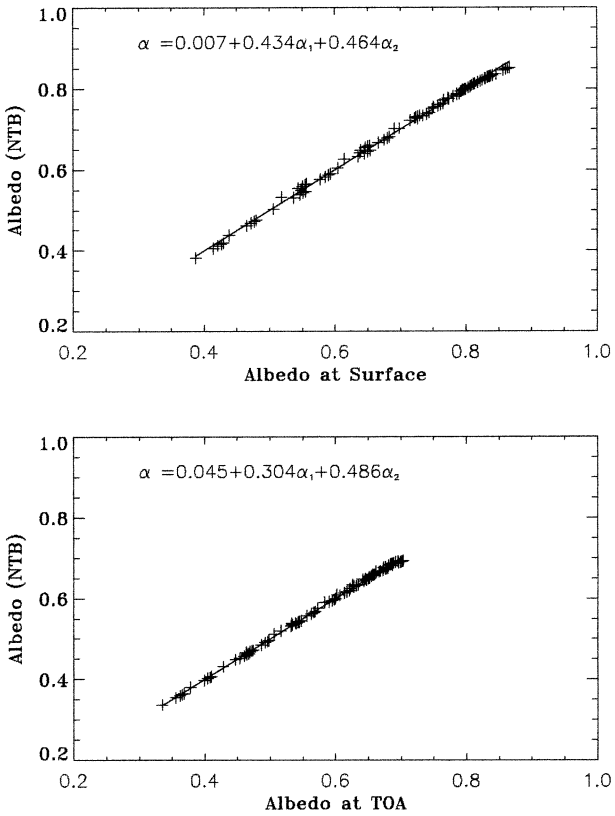

FIG. 2. NTBC relations derived by linear regression using model-simulated narrow and broadband albedos (top) over snow surface and (bottom) at the TOA. In model simulations, the snow grain sizes are assumed to vary from 50 to 2000 μm and solar zenith angles vary from 30° to 70° (total point number $N = 90$). The x axis is the measured broadband albedo and the y axis is the derived broadband albedo via NTBC.

a high value is indicative of melting snow, ice, or ponds. This empirical formula shows that, with the melt of snow and ice, γ will increase. Thus, the NTBC coefficient for the visible increases while that for the NIR decreases. In fact, Eq. (8) is completely consistent with Eqs. (4)–(6). Picking values of γ equal to 0.09, 0.1, and 0.06 reproduces Eqs. (4)–(6), respectively. In the measurements of Perovich et al. (1999), the average of γ is 0.102 and the standard deviation is 0.035. The value $\gamma = 0.06$ corresponds to using fine-grained new snow in our model simulations. Equation (8) is consistent with the relation of Lindsay and Rothrock (1994) if $\gamma = 0.06$, implying that their measurements were taken over a snow-covered ice surface. If $\gamma = 0.15$, then Eq. (8) is consistent with the relation of Stroeve et al. (1997) obtained from measurements on the Greenland ice sheet. This value is high and should correspond to melting snow or ice. However, it is understandable because the albedo values of Stroeve et al. represent a variety of snow types that range from fine-grained new snow to coarse-grained melting snow (Stroeve et al. 1997). Thus, Eq. (8) provides a general NTBC relationship that can be used to derive improved broadband albedo over snow and ice surfaces during the melt season in the Arctic.

The error of the derived broadband albedo is large when the albedo in channel 2 is much less than in channel 1. This is the case for melting snow, ice, and ponds. For example, when $\alpha_2 = 0.6\alpha_1$ ($\gamma = 0.25$) and α_1 lies in the range between 0.4 and 0.75, the broadband albedo derived from the relation of Stroeve et al. (1997) is 23% larger than that derived from the relation of Lindsay and Rothrock (1994). Equation (8) yields an albedo that is about 34% larger than that derived from the relation of Lindsay and Rothrock (1994). On the other hand, when $\alpha_2 = 0.9\alpha_1$ ($\gamma = 0.053$) and α_1 lies in the range between 0.6 and 0.95, which corresponds to fine-grained snow, the broadband albedo resulting from Eq. (8) is very close to that derived from the relation of Lindsay and Rothrock (1994), whereas the relation of Stroeve et al. (1997) yields a broadband albedo that is higher by 7%. Therefore, we believe that an NTBC relation that takes into account the snowmelt condition is required for deriving reliable albedo values throughout the melt season in the polar regions. In the remainder of this paper, the NTBC relation given in Eq. (8) will be used to derive the broadband albedo unless otherwise specifically mentioned.

3. Uncertainty analysis

a. Effect of aerosols, ozone, and water vapor

Lindsay and Rothrock (1994) pointed out that sparse data on aerosols, ozone, and water vapor in the atmospheric column led to uncertainty in the albedo of 0.13, 0.04, and 0.08, respectively, but the uncertainties in monthly average albedos were not as large. The uncertainties estimated by Stroeve et al. (1997) are much smaller. They showed that for a 50% uncertainty in the aerosol amount the errors for the visible channel can be as large as 3.3%, whereas for a 50% uncertainty in the ozone amount the error can be as large as 1.5%. The uncertainties in the water vapor amount have the smallest effect as compared with aerosol and ozone. Contemporaneous estimation of these variables could reduce the uncertainty in the estimated albedo considerably, but retrieval of aerosol properties over snow and ice surfaces from AVHRR is very difficult. Only water vapor data are available from sounding profiles, so we examined the effects of using such profiles on the retrieval of albedo from the RTM. Figure 3 shows the reflectance of channels 1 and 2 as a function of surface albedos for two different atmospheric profiles. The higher the albedo is, the larger the difference is between reflectances derived from summer and winter profiles. The influence of using different atmospheric water vapor profiles is much smaller in channel 1 than in channel 2. For surface albedo values between 0.5 and 0.8, the reflectance difference in channel 1 is less than 5%, whereas in channel 2, the difference is about 15%–25%. Note that the total

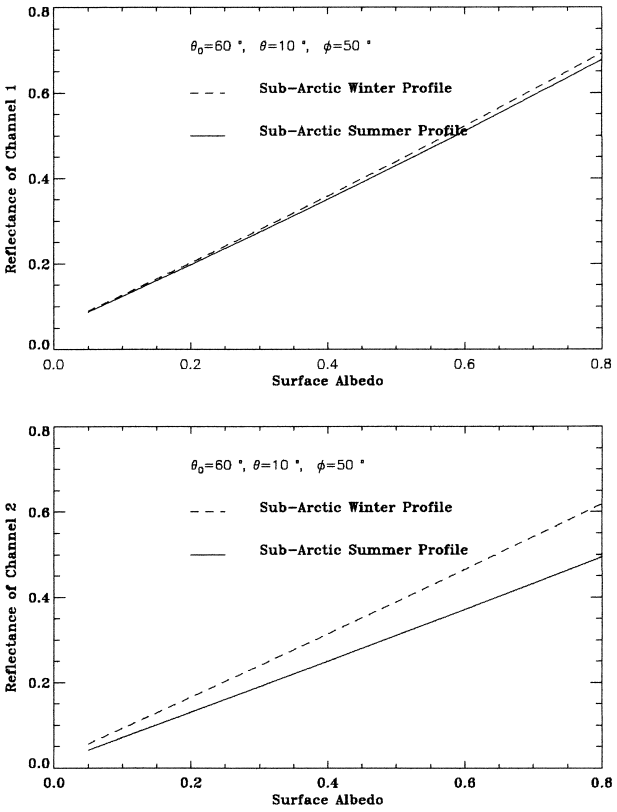

FIG. 3. Simulated reflectance at the TOA for AVHRR channels (top) 1 and (bottom) 2 as a function of surface albedo for subarctic summer (solid line) and subarctic winter (dashed line) atmospheric profiles under the condition of $\theta_0 = 60°$, $\theta = 10°$, and $\phi = 50°$.

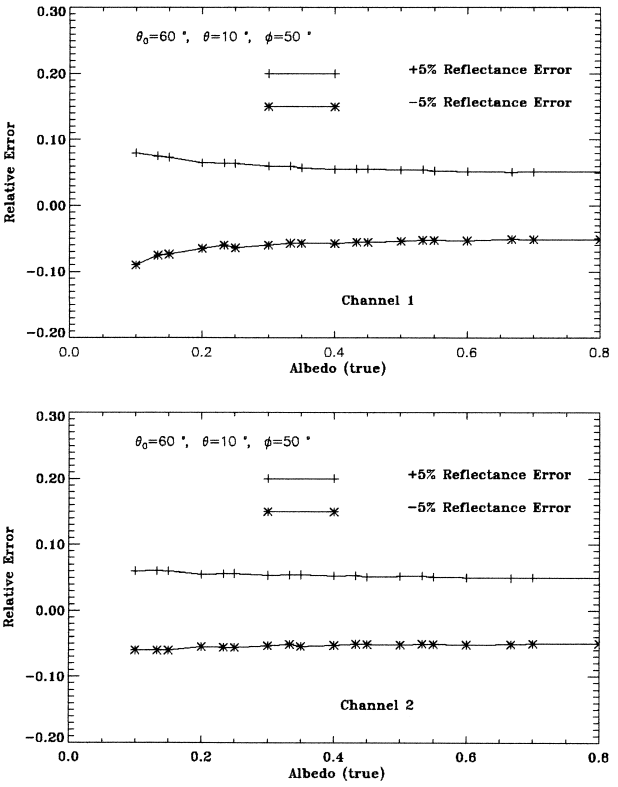

FIG. 4. Error of the retrieved narrowband albedo for AVHRR channels (top) 1 and (bottom) 2 for an uncertainty of +5% (+) and −5% (*) in satellite-measured radiance in these two channels under the condition of $\theta_0 = 60°$, $\theta = 10°$, and $\phi = 50°$.

amount of water vapor is four times larger for subarctic summer than for subarctic winter. Hence, use of water vapor data from realistic climatological values based on sounding data will improve the precision of the albedo retrieval in channel 2. This method is especially important because the amount of water vapor in the atmosphere changes significantly as the surface evolves from dry snow to melting snow and ice in the Arctic during summer.

b. Satellite measurements

Comparison of the retrieved spectral albedo in channels 1 and 2 with the input albedo used to generate the reflectances in the lookup tables is shown in Fig. 4. The *x* axis is the true albedo in channels 1 and 2, and the *y* axis is the relative error of the retrieved albedo. For a ±5% error in the reflectance in channels 1 and 2, the error in the retrieved albedo is about 5% for both channels 1 and 2 when $\theta_0 = 60°$, $\theta = 10°$, and $\phi = 50°$. Only when the albedo is smaller than 0.1 does the error become a little larger. The uncertainty in the broadband albedo is about 5%–10%.

c. Effect of snow bidirectional reflectance

To examine the effect of bidirectional snow reflectance on the retrieval of albedo, we compared the model-simulated narrowband albedo computed from our RTM for the coupled atmosphere–snow (non-Lambertian snow surface) system with that retrieved from our albedo retrieval algorithm, in which a Lambert surface is used.

The reflectances in channels 1 and 2 were computed using the RTM for the coupled atmosphere–snow system for a series of values of snow grain size and impurities (mass fraction of soot). With these reflectances as inputs to our albedo retrieval algorithm, we obtained the retrieved albedo over the snow surface. The corresponding true albedo values of the snow surfaces were calculated directly from our RTM for the coupled atmosphere–snow (non-Lambertian snow surface) system as the ratio of upward irradiance to downward irradiance at the snow surface. Comparison of the narrowband retrieved albedos with the true albedos is shown in Fig. 5. On average, the narrowband albedo in channel 1 (upper panel) is underestimated by 1.5% when $\theta_0 = 60°$, $\theta = 10°$, and $\phi = 50°$ and is overestimated by 9.5% when $\theta = 30°$ and $\phi = 150°$. On the other hand, when $\theta = 10°$ and $\phi = 50°$, the narrowband albedo in channel

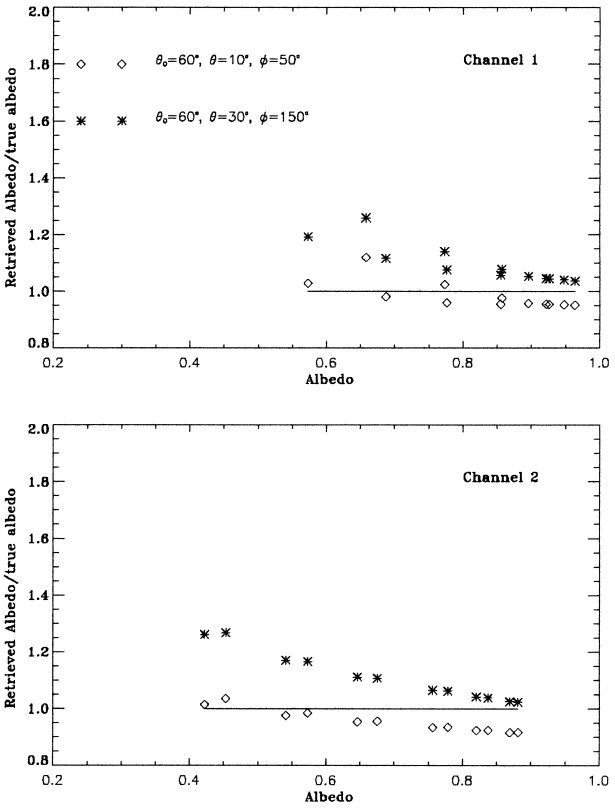

FIG. 5. Ratio of the retrieved narrowband albedo for Lambertian surfaces to the actual snow albedo in channels (top) 1 and (bottom) 2 under the different condition of $\theta_0 = 60°$, $\theta = 10°$, and $\phi = 50°$ ($\diamond$) and $\theta_0 = 60°$, $\theta = 30°$, and $\phi = 150°$ (*). The x axis is the model output albedo over snow surface for a variety of snow grain size and mass fraction of soot, and albedo retrieval uses the model output reflectances in channels 1 and 2 at the TOA.

2 (lower panel) is underestimated by 4.5%, and, when $\theta = 30°$ and $\phi = 150°$, the albedo in channel 2 is overestimated by 11.1%.

As the anisotropic factor becomes larger for larger polar and azimuthal angles (see Fig. 1 of Han et al. 1999), the effect of snow bidirectional reflectance causes the reflectance in channels 1 and 2 to be larger (or smaller) for a snow surface than for a Lambert reflector. Thus the retrieved albedo in channels 1 and 2 will be overestimated or underestimated. From our calculations we have found that the maximum errors for channels 1 and 2 are 3.5% and 10%, respectively, when $\theta = 10°$, $\phi = 50°$, and $\theta_0 = 60°$. When $\theta = 30°$, $\phi = 150°$, and $\theta_0 = 60°$, the error can be as high as 26% and 27% for channels 1 and 2, respectively. From these calculations it can be concluded that, when the viewing angle is small ($\theta < 10°$), the uncertainty in the retrieved broadband albedo is less than 5% if the effect of bidirectional reflectance is ignored, but it can be more than 20% for $\theta = 30°$. In our analysis of SHEBA data, only the near-overhead passes with small viewing angles are chosen. Thus, our albedo retrieval errors from ignoring the snow bidirectional reflectance effects after 10 June are less than about 5%–10%.

4. Application and results

a. SHEBA surface measurements and satellite data

SHEBA is a coordinated program to address the interaction of surface energy balance, atmospheric radiation, and clouds over the Arctic Ocean, focusing on the key processes that determine ice albedo feedback in the Arctic pack ice. The Canadian Coast/Guard icebreaker *Des Groseilliers* was used as a floating station deployed in the Arctic Ocean at 75°16.3′N, 142°41.2′W and left to drift for a year. The SHEBA ice camp drifted considerably northwestward, and it was at 78.5°N, 166°W by the end of July of 1998. One full year of measurements was obtained at the ice camp from October of 1997 to October of 1998. These measurements include surface-based radiation measurements, atmospheric profiling by balloonborne sounding systems, radar and lidar systems, and observations of clouds by several different instruments. One goal of SHEBA is to extend the process-oriented observations and models to larger scales. A detailed description of surface albedo measurements obtained at SHEBA is provided by Perovich et al. (1999). These measurements were taken along a 200-m survey line (instead of at one point) throughout the melting season at the SHEBA ice camp. The spectral and wavelength-integrated albedos were measured at least weekly every 2.5 m from October through April. From June through August, albedo measurements were made every other day. Albedos were accurate to within ± 0.01 (Perovich et al. 1999).

Because no postlaunch calibration of AVHRR channels 1 and 2 is performed on National Oceanic and Atmospheric Administration (NOAA) satellite *NOAA-12*, we used *NOAA-14* AVHRR data with 1.1-km pixel resolution for our retrieval of albedo. The revised postlaunch calibration by Rao and Chen (1999) is used instead of the calibration by Rao and Chen (1996). To reduce the bidirectional effects, one to three overpasses per day near local noon at SHEBA between mid-April and the end of August of 1998 were processed to retrieve the albedo. This time of AVHRR overpasses is not exactly coincident with the time of surface measurement of albedo. The spatial coverage used to retrieve albedo is 100×100 pixels with the center over the SHEBA ice camp. The albedos for all clear pixels are retrieved, and their average values are used for comparison with the in situ measurements.

b. Detection of clouds

Accurate identification of clear pixels from the AVHRR images is required for reliable albedo retrieval. Contamination of cloud pixels could result in an overestimate of albedo, because the reflectance over cloud

is normally larger than over snow or ice. This fact is because the cloud droplet size is smaller than the size of snow crystals. Cloud shadows over snow and ice will result in an underestimate of the albedo determined from space. An automatic cloud discrimination method developed by Xiong (2000) is used, in which clear pixels are identified if the solar reflectance in channel 3 is lower than a certain threshold and the pixels are determined to belong to one of several surface types associated with the Arctic Ocean. Because of the strong bidirectional reflectance, Xiong (2000) derived the actual albedo r_3 at the TOA (anisotropy-corrected albedo) from satellite measurements by dividing the isotropic reflectance by the anisotropic reflectance factor. A threshold function for r_3 [a second-order polynomial in $\sec(\theta_0)$] is used together with the brightness temperature difference between channels 4 and 5 (BTD45) for cloud detection. BTD45 was used to discriminate thin ice clouds from snow and ice surfaces. Use of this algorithm with AVHRR daytime data between mid-April and the end of August of 1998 yields AVHRR cloud-cover fractions consistent with SHEBA surface measurements with an error of no more than 10%.

c. *Seasonal variation of surface albedo over SHEBA from AVHRR and its comparison with SHEBA surface measurements*

Figure 6 shows the albedo retrieved from *NOAA-14* AVHRR data obtained over SHEBA between the middle of April and the end of August of 1998. The observed surface albedo reported by Perovich et al. (1999) is also shown in this figure. The *NOAA-14* AVHRR data are from the Atmospheric Radiation Measurement Program (ARM) archive, but recalibrations are made using the revised calibration coefficients of Rao and Chen (1999). In general, one to three AVHRR overpasses are used per day subject to the conditions that the solar zenith angle be less than 70° and the viewing angle be small. Thus, overpasses used in this study normally take place around local noon. Between 23 June and 3 July 1998 no data are available. No suitable overpasses were found between 1 and 4 August 1998 either. The values of albedo shown in the figure represent an average albedo for all clear pixels in the image of size 100 × 100 pixels. When computing the average we did not use pixels for which the albedo deviates from the average by more than 3 times the standard deviation of this image. This filter helps to compensate for possible errors in the cloud mask by disregarding cloudy pixels whose albedo is higher than that of the surface. When the number of pixels remaining is larger than 50, the average albedo is regarded as valid and is plotted in this figure. The total number of overpasses was $N = 129$. The number of surface measurements is normally once every other day after June (Perovich et al. 1999). The surface albedo is also taken to be the average for all measurements along the 200-m survey line. Further comparison of

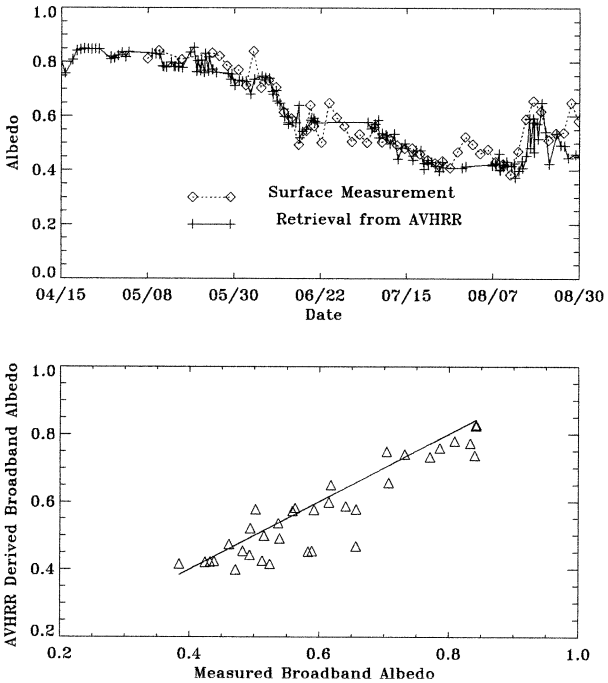

FIG. 6. (top) Seasonal variation of broadband albedo derived from *NOAA-14* AVHRR 1.1-km data with the center in the SHEBA ice camp and its comparison with SHEBA surface measurements (bottom). The comparison of surface-measured albedo with that derived from AVHRR in the same day. Averages are taken for all clear pixels in each AVHRR image (100 × 100 pixels) and for all surface measurements along the 200-m survey line.

satellite-retrieved broadband albedo and surface-measured broadband albedo on a day-by-day basis is shown in the lower panel of Fig. 6 for satellite overpasses near local noon. The difference between them is less than 7%, on average. Considering that the times and locations are not exactly the same, the agreement is very good. Figure 7 shows a color image of the albedo retrieved from a *NOAA-14* AVHRR overpass on 2241 UTC 23 May 1998 (left panel) and 1845 UTC 20 July 1998 (right). The black area is cloudy. The image size is 100 × 100 pixels, with the SHEBA ice camp in the center of the image. A large spatial variation of albedo is evident in this image. The albedo ranges from 0.45 to 0.89 with a mean of 0.85 and a standard deviation 0.04 for the left image on 23 May 1998. It ranges from 0.27 to 0.50 with a mean of 0.43 and a standard deviation of 0.02 for the right image on 20 July 1998. Because the snow on the ice has not started to melt on 23 May, the albedo is high. The area of low albedo is leads, which is obvious from the image. The albedo is much lower on 20 July than on 23 May because of the melting of snow and ice. As mentioned before, we made an anisotropic correction to the albedo on 23 May but not on 20 July. The difference between albedo values obtained with and without anisotropic correction is 9.6% on average for the whole season. We also compared the difference incurred by using different NTBC relations. On

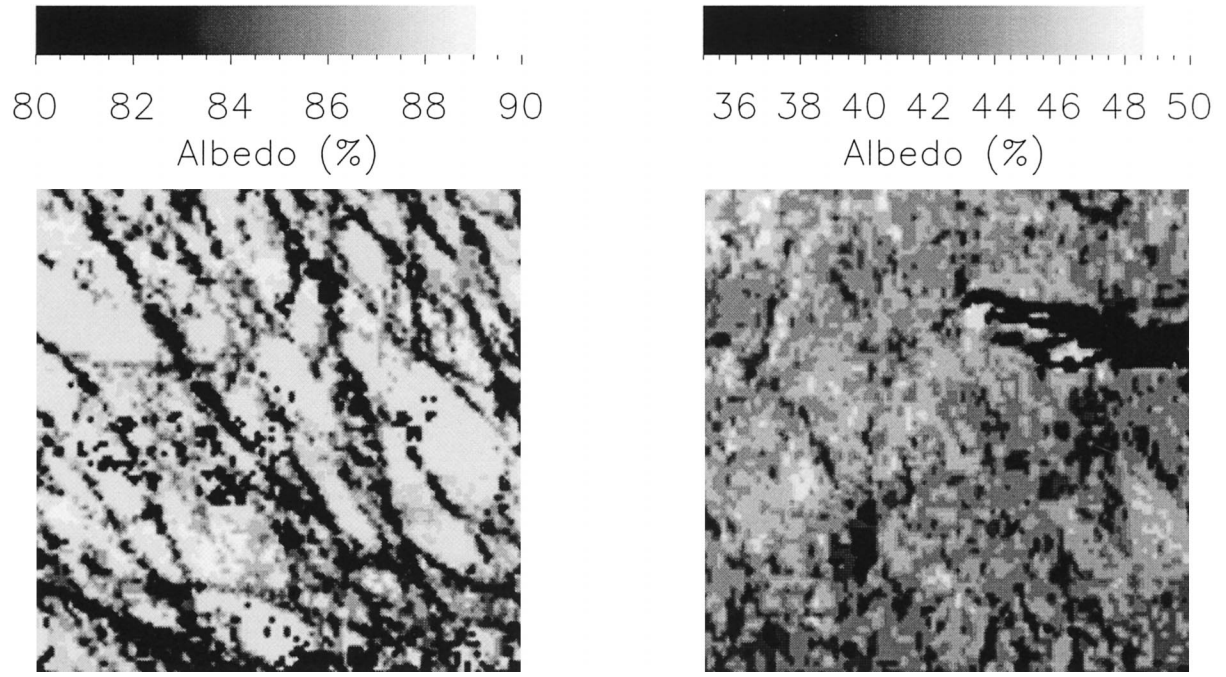

FIG. 7. Color image of satellite-derived broadband albedo for overpass on (left) 2241 UTC 23 May 1998 and (right) 1845 UTC 20 Jul 1998 over the SHEBA ice camp. Black error in right panel is covered cloud.

average, the albedo obtained by using the NTBCs of Stroeve et al. (1997) overestimates the albedo by 7.9% when compared with that obtained from Eq. (8).

Comparison of satellite-derived and surface-measured albedo in Fig. 6 shows that, overall, the satellite retrieval has captured the seasonal variation of the albedo. Before June, the albedo is high and stable. With the onset of melting, surface conditions evolved from dry snow (before May), to melting snow (early June), to early melt ponds (late June), to fully developed melt ponds (middle of July), and the albedo decreases from about 0.85 to 0.4. After the middle of August, the albedo starts to increase. In general, the albedo shows a gradual evolution due to seasonal transitions and abrupt shifts resulting from synoptic weather events that cause the onset of snow and melt quickly (Perovich et al. 1999). Because the albedo derived from AVHRR data is the average albedo over a large area, however, it does not exhibit some of the abrupt shifts in albedo due to synoptic weather events: for example, snow precipitation, which leads to an increase in albedo, or rain precipitation, which leads to a decrease of albedo when dry snow becomes wet. These albedo differences corresponding to the spikes in the figure are understandable because of the much larger spatial coverage of the satellite and because the synoptic process is always of limited temporal duration and spatial extent. Also, albedo retrieval from space is not possible when the surface is obscured by clouds, and misidentification of clear sky will lead to some error in the albedo retrieval. In view of the large spatial variation in albedo (see Fig. 7), the agreement between satellite-retrieved and surface-measured albedo is reasonable. Large spatial variation of albedo along the 200-m survey line was also found by Perovich et al. (1999). The agreement is relatively less satisfactory after the middle of August. Large variation of albedo after August, due to developed ponds and leads, resulting in a very inhomogeneous surface, is the prime reason for the disagreement.

5. Summary and conclusions

An algorithm to retrieve the narrowband surface albedo from AVHRR data in channels 1 and 2 was developed based on a rigorous radiative transfer model. The broadband albedo is obtained from narrow-to-broadband conversion of the narrowband albedos. We find that different surface–atmosphere conditions lead to different NTBC coefficients, however. This empirical finding is supported by radiative transfer simulations.

Uncertainties in the retrieval of narrowband albedo are caused by uncertainties in the radiometric calibrations of the satellite sensors and the sparsity of data on aerosols, ozone, and water vapor. A $\pm 5\%$ error in radiometric calibrations could result in an albedo uncertainty of about 5%–10%. A large uncertainty in the calibration of AVHRR channels 1 and 2 is one of the most vexing problems with the application of such data. Water vapor has an important impact on channel 2 radiance, and use of a subarctic summer profile instead of a winter profile can lead to the difference of $\pm 15\%$–25% in the reflectance over a snow surface because

AVHRR channel 2 (0.72–1.10 μm) covers the strong water vapor absorption band at 0.94 μm. Thus, water vapor absorption is significant in channel 2, and the optical depth due to water vapor absorption in the lower atmosphere is almost 2 times as large in summer as in winter. This difference will cause a significant error in the retrieved albedo because the amount of water vapor in the Arctic changes greatly with the onset of melt and as the melting of snow and ice progresses. In this paper, we used the subarctic summer atmospheric profile, but the water vapor amount is obtained from sounding profiles. The aerosol amount is adopted from the tropospheric background aerosol model in MODTRAN. So, the error in the albedo retrieval due to our choice of clear-sky (molecular) atmospheric parameters is small, but the uncertainties associated with the lack of precise knowledge of aerosol optical properties may be larger.

The NTBC coefficients vary considerably with different surface and atmospheric conditions. As the snow begins melting, the coefficient for channel 1 increases while that for channel 2 decreases. Use of different NTBCs may result in a broadband albedo uncertainty of about 5%–10%. The conversion coefficients depend on both the atmosphere and surface physical conditions. Thus, situation-specific NTBC coefficients that can be obtained from surface measurements should be used.

For the retrieval of albedo over snow surfaces, use of the Lambertian assumption is generally not appropriate. Because of the bidirectional reflectance of snow/ice surfaces, use of the Lambert assumption results in an overestimate of the albedo for measurements obtained in the forward direction and an underestimate of the albedo for measurements obtained in the backward direction. For θ less than 10°, the error in the albedo is less than 5%–10%, however, whereas for θ greater than 30° and large azimuthal angles, the error in the albedo is large because of the large bidirectional reflectance. This fact is why we chose the near-overhead passes of AVHRR for analysis. Anisotropic correction to the albedo using model-simulated ARFs for snow surfaces is possible, however (Jin and Simpson 2000; Stroeve et al. 1997). Such a correction increases the precision of the albedo retrieval over snow surfaces and was made for the measurements taken before 10 June 1998.

NOAA-14 AVHRR data obtained over the SHEBA ice camp were used to retrieve the surface albedo between mid-April and the end of August of 1998. Large spatial and seasonal variations in the albedo were found. Comparison of the AVHRR-retrieved surface albedo for this period with the albedo determined from direct albedo measurements at SHEBA shows that the albedo retrieved from the AVHRR data is in good agreement with that measured at the surface. Minor differences between them are due mainly to differences in spatial coverage and to the large variation in surface albedo due to the development of melt ponds and leads. Failure to discriminate thin or cirrus cloud from the snow surface may lead to a significant error in albedo retrieval from space. With the deployment of new sensors, such as the moderate-resolution imaging spectroradiometer (MODIS) on the National Aeronautics and Space Administration *Terra* and Aqua satellites, many additional channels become available. These new channels should lead to improved albedo retrieval in the Arctic because it becomes possible to improve the cloud discrimination. For example, the 1.38-μm channel of MODIS is expected to improve the discrimination of ice clouds. Also, ''real-time'' temperature and water vapor data will become available from the atmospheric infrared sounder, to be launched on the Aqua satellite with MODIS. Use of such data in conjunction with AVHRR or MODIS data will lead undoubtedly to improved retrievals of albedo from space.

Acknowledgments. This research was supported by the National Science Foundation as part of the SHEBA program under NSF-OPP-970184, and by the ARM Program sponsored by the U.S. Department of Energy, Office of Science, Office of Biological and Environmental Research, Environmental Sciences Division. AVHRR data were obtained through the ARM Program. Surface albedo measurements over SHEBA were provided by Dr. D. Perovich.

REFERENCES

Allison, I., R. E. Brandt, and S. G. Warren, 1993: East Antarctic sea ice: Albedo, thickness distribution, and snow cover. *J. Geophys. Res.,* **98,** 12 417–12 429.

Anderson, G. P., S. A. Clough, F. X. Kneizys, J. H. Chetwynd, and E. P. Shettle, 1986: AFGL Atmospheric Constituent Profiles (0–120 km). Air Force Geophysics Laboratory Tech. Rep. AFGL-TR-86-0110 (OPI), 43 pp.

Aoki T., T. Aoki, M. Fukabori, A. Hachikubo, Y. Tachibana, and F. Nishio, 2000: Effects of snow physical parameters on spectral albedo and bidirectional reflectance of snow surface. *J. Geophys. Res.,* **105,** 10 219–10 236.

Blanchet, J., and R. List, 1983: Estimation of optical properties of Arctic haze using a numerical model. *Atmos.–Ocean,* **21,** 444–465.

Briegleb, B. P., P. Minnis, V. Ramanathan, and E. Harrison, 1986: Comparison of regional clear-sky albedos inferred from satellite observations and model calculations. *J. Climate Appl. Meteor.,* **25,** 214–226.

Clarke, A. D., and K. J. Noone, 1985: Soot in the Arctic snowpack: A cause for perturbations in radiative transfer. *Atmos. Environ.,* **19,** 2045–2053.

Csiszar, C., and G. Gutman, 1999: Mapping global land surface albedo from NOAA AVHRR. *J. Geophys. Res.,* **104,** 6215–6228.

Curry, J. A., W. B. Rossow, D. Randall, and J. L. Schramm, 1996: Overview of Arctic cloud and radiation characteristics. *J. Climate,* **9,** 1731–1764.

De Abreu, R. A., J. Key, J. A. Maslanik, M. C. Serreze, and E. F. LeDrew, 1994: Comparison of in situ and AVHRR-derived broadband albedo over Arctic sea ice. *Arctic,* **47,** 288–297.

Han, W., K. Stamnes, and D. Lubin, 1999: Remote sensing of surface and cloud properties in the Arctic from NOAA AVHRR measurements. *J. Appl. Meteor.,* **38,** 989–1012.

Jin, Z., and J. J. Simpson, 1999: Bidirectional anisotropic reflectance of snow and sea ice in AVHRR channels 1 and 2 spectral regions—Part I: Theoretical analysis. *IEEE Trans. Geosci. Remote Sens.,* **37,** 543–554.

——, and ——, 2000: Bidirectional anisotropic reflectance of snow and sea ice in AVHRR channels 1 and 2 spectral regions—Part II: Correction applied to imagery of snow on sea ice. *IEEE Trans. Geosci. Remote Sens.,* **38,** 999–1015.

Knap, W. H., and J. Oerlemans, 1996: The surface albedo of the Greenland ice sheet: Satellite-derived and in situ measurement in the Sondre Stromfjord and during the 1991 melt season. *J. Glaciol.,* **42,** 364–374.

——, B. W. Brock, J. Oerlemans, and I. C. Wills, 1999: Comparison of Landsat TM-derived and ground-based albedos of Hunt Glacier d'Arolla, Switzerland. *Int. J. Remote Sens.,* **20,** 3293–3310.

Koepke, P., 1989: Removal of atmospheric effects from AVHRR albedos. *J. Appl. Meteor.,* **28,** 1344–1348.

Langleben, M. P., 1971: Albedo of melting sea ice in the southern Beaufort Sea. *J. Glaciol.,* **10,** 101–104.

Li, Z., and H. G. Leighton, 1992: Narrowband to broadband conversion with spatially autocorrelated reflectance measurement. *J. Appl. Meteor.,* **31,** 421–433.

Lindsay, R. W., and D. A. Rothrock, 1994: Arctic sea ice albedo from AVHRR. *J. Climate,* **7,** 1737–1749.

Lubin, D., and P. J. Weber, 1995: The use of cloud reflectance functions with satellite data for surface radiation budget estimation. *J. Appl. Meteor.,* **34,** 1333–1347.

McClatchey, R. A., R. W. Fenn, J. E. A. Selby, F. E. Volz, and J. S. Garing, 1971: Optical properties of the atmosphere. Air Force Cambridge Research Laboratory Rep. AFCRL-71-0279, 85 pp.

Penndorf, R., 1957: Tables of the refractive index for standard air and the Rayleigh scattering coefficient for the spectral region between 0.2–20 μm and their application to atmospheric optics. *J. Opt. Soc. Amer.,* **47,** 176–182.

Perovich, D. K., and Coauthors, 1999: SHEBA. *Snow and Ice Studies,* CRREL, CD-ROM. [Available from D. Perovich, CRREL, 72 Lyme Road, Hanover, NH 03755.]

Rao, C. R. N., and J. Chen, 1996: Post-launch calibration of the visible and near-infrared channels of the Advanced Very High Resolution Radiometer on the *NOAA-14* spacecraft. *Int. J. Remote Sens.,* **17,** 2743–2747.

——, and ——, 1999: Revised post-launch calibration of the visible and near-infrared channels of the Advanced Very High Resolution Radiometer (AVHRR) on the *NOAA-14* spacecraft. *Int. J. Remote Sens.,* **20,** 3485–3491.

Saunders, R. W., 1990: The determination of broad band surface albedo from AVHRR visible and near-infrared radiances. *Int. J. Remote Sens.,* **11,** 49–67.

Song, J., and W. Gao, 1999: An improved method to derive surface albedo from narrowband AVHRR satellite data: Narrowband to broadband conversion. *J. Appl. Meteor.,* **38,** 239–249.

Stamnes, K., 1982: Reflection and transmission by a vertically inhomogeneous planetary atmosphere. *Planet. Space Sci.,* **30,** 727–732.

——, S. C. Tsay, W. Wiscombe, and K. Jayaweera, 1988: Numerically stable algorithm for discrete-ordinate-method radiative transfer in multiple scattering and emitting layered media. *Appl. Opt.,* **27,** 2502–2509.

——, R. G. Ellingson, J. A. Curry, J. E. Walsh, and B. D. Zak, 1999: Review of science issues and deployment strategies for the north slope of Alaska/adjacent Arctic Ocean (NSA/AAO) ARM site. *J. Climate,* **12,** 1413–1423.

Stroeve, J., A. Nolin, and K. Steffen, 1997: Comparison of AVHRR-derived and in situ surface albedo over the Greenland ice sheet. *Remote Sens. Environ.,* **62,** 262–276.

——, E. B. Box, C. Fowler, T. Haran, and J. Key, 2001: Intercomparison between in situ and AVHRR Polar Pathfinder–derived surface albedo over Greenland. *Remote Sens. Environ.,* **75,** 360–374.

Suttles, J. T., and Coauthors, 1988: Angular radiation models for earth–atmosphere system. Vol. 1, Shortwave radiation, NASA Ref. Pub. 1184, 144 pp.

Taylor, V. R., and L. L. Stowe, 1984: Atlas of reflectance patterns for uniform earth and cloud surfaces (NIMBUS-7ERB-61 days). NOAA Tech. Rep. NESDIS 10, 66 pp.

Thomas, G. E., and K. Stamnes, 1999: *Radiative transfer in the Atmosphere and Ocean.* Cambridge University Press, 517 pp.

Toll, D. L., D. Shirey, and D. S. Kimes, 1997: NOAA AVHRR land surface albedo algorithm development. *Int. J. Remote Sens.,* **18,** 3761–3796.

Tsay, S. C., K. Stamnes, and K. Jayaweera, 1989: Radiative energy budget in the cloudy and hazy Arctic. *J. Atmos. Sci.,* **46,** 1002–1017.

——, ——, and ——, 1990: Radiative transfer in stratified atmospheres: Development and verification of a unified model. *J. Quant. Spectrosc. Radiat. Transfer,* **43,** 133–148.

Warren, S. G., 1982: Optical properties of snow. *Rev. Geophys. Space Phys.,* **20,** 67–89.

——, and W. J. Wiscombe, 1980: A model for the spectral albedo of snow. II: Snow containing atmospheric aerosols. *J. Atmos. Sci.,* **37,** 2734–2745.

Xiong, X., 2000: Cloud and surface properties and the solar radiation budget derived from satellite data over the Arctic Ocean: Comparison with surface measurements and in situ aircraft data. Ph.D dissertation, University of Alaska Fairbanks, 217 pp.